Ferromagnetic resonance saturation and second order Suhl spin wave instability processes in thin Permalloy films

Heidi M. Olson,[a] Pavol Krivosik,[b] Kumar Srinivasan,[c] and Carl E. Patton
Department of Physics, Colorado State University, Fort Collins, Colorado 80523

(Received 9 February 2007; accepted 6 June 2007; published online 18 July 2007)

High power ferromagnetic resonance (FMR) loss versus static field H profiles and the corresponding spin wave instability threshold microwave field amplitude h_{crit} vs H butterfly curves were measured for in-plane magnetized thin Permalloy films of thicknesses 35, 57, 74, 104, and 123 nm at a nominal pumping frequency of 9.11 GHz. Cavity loading and calibration issues that proved to be problematic in past attempts to obtain accurate resonance saturation data over the full FMR profile in ferrites and metal films were resolved through a careful decoupling of the pump field and a full cavity response calibration. The FMR profiles show a drop in the loss peak, a shift in the peak to lower field, a broadening, and the development of a foldover-like asymmetry as the power is increased. The butterfly curves show a minimum h_{crit} at the low power FMR field and a smooth rounded increase on either side, except for a small kink on the low field side associated with the shift and asymmetry development. Apart from the kink, the second order Suhl spin wave instability theory, suitably modified for thin films, provided good fits to the butterfly curve data through the use of a single spin wave linewidth ΔH_k value for each data set. The ΔH_k values ranged from 16 to 35 Oe, with the implied critical mode in-plane wave vectors always directed parallel to the static field. These spin wave linewidths translate into Gilbert damping parameter α_k values in the 0.002–0.005 range, the same order as expected for intrinsic magnon-electron scattering losses in metal ferromagnets. These α_k values are about a factor of 2 smaller than those implied by the low power FMR linewidths. The FMR in-plane precession cone angles at threshold were on the order of 3°–6°. © *2007 American Institute of Physics*. [DOI: 10.1063/1.2756481]

I. INTRODUCTION

Dobin and Victora[1] have recently demonstrated a direct connection between the nonlinear dynamics in large angle magnetization switching in thin films and parametric Suhl spin wave instability processes.[2] The additional losses associated with these nonlinear processes can, in principle, have a dramatic effect on magnetization switching in recording applications. The extra losses, for example, can serve to reduce switching speeds in conventional heads and media applications. At the same time, the nonlinear interactions can also promote magnetization reversal. This has been recently demonstrated for a variety of current driven nanocontact and nanopillar spin torque devices.[3,4]

One clear way to examine the basic nonlinear interactions that are relevant to large angle switching in thin films is to study the Suhl second order spin wave instability processes that occur at ferromagnetic resonance (FMR) for high microwave power levels. While high power FMR experiments do not extend to angles as large as those that occur in switching, they provide a measure of the precession angles at which nonlinear effects come into play. In Permalloy films, for example, the onset of Suhl spin wave instability (SWI) processes and resonance saturation effects generally occur at precession angles in the 3°–6° range.

While there has been extensive work on Suhl processes in ferrites, high power FMR work on metal films is limited to a few studies in the 1960s. High power resonance saturation for in-plane magnetized Permalloy films was first observed by Comly *et al.*[5] Follow-up work by Berteaud and Pascard[6,7] revealed resonance saturation at high power as well as evidence for the so-called subsidiary absorption at lower fields associated with Suhl first order processes. All of these early data were somewhat limited in focus and there were no quantitative connections to the Suhl theory.

Recent work by An *et al.*[8] extended measurements of subsidiary absorption to include full data on the Suhl SWI threshold microwave field amplitude versus static field for in-plane magnetized films. These authors also provided a full analysis of the data based on the Suhl first order theory, suitably modified for the thin film geometry. As a result of cavity loading and calibration issues, Ref. 8 did not include any quantitative work on resonance saturation or Suhl second order processes.

This work is concerned specifically with the quantitative study of the high power resonance saturation response for thin Permalloy films. The cavity loading and calibration issues from Ref. 8 have been resolved. The sections below give a full description of the experimental methods, present comprehensive data on resonance saturation, and provide a theoretical analysis of the relevant Suhl processes over the full FMR profile. The main results are (1) FMR profiles as a function of input power, (2) a determination of the SWI threshold microwave field amplitude (h_{crit}) as a function of

[a]Electronic mail: heidio@lamar.colostate.edu
[b]On leave from the Department of Electromagnetic Field Theory, Faculty of Electrical Engineering and Information Technology, Bratislava, Slovakia.
[c]Present address: Spintronics, Media and Interface Division, Data Storage Institute, Singapore.

 © 2007 American Institute of Physics

Downloaded 26 Jul 2007 to 129.82.208.99. Redistribution subject to AIP license or copyright, see http://jap.aip.org/jap/copyright.jsp

TABLE I. Summary of low power 9.11 GHz ferromagnetic resonance (FMR) measurements and derived parameters.

Film thickness d (nm)	FMR field H_{FMR} (Oe)		Effective saturation induction $4\pi M_{s\text{-}eff}$ (G)	Gyromagnetic constant $\lvert\gamma\rvert/2\pi$ (MHz/Oe)	IPSF half power FMR linewidth ΔH_{FMR} (Oe)	IPSF equivalent Gilbert damping parameter α_{FMR}
	In-plane static field (IPSF)	Perpendicular-to-plane static field (PPSF)				
35	806	13 878	10 820	2.976	44	0.0072
57	838	13 591	10 510	2.954	41	0.0066
74	782	14 275	11 210	2.974	37	0.0060
104	830	14 494	11 320	2.869	59	0.0093
123	850	13 560	10 460	2.938	56	0.0090

the static magnetic field (H) over the entire FMR profile, and (3) an analysis of the h_{crit} vs H data in terms of the second order Suhl theory. Such h_{crit} vs H profiles are termed butterfly curves. Item (3) yields the critical modes and spin wave damping parameters applicable to resonance saturation. These results represent the first comprehensive measurements and analyses of Suhl processes at FMR for metal films. They also represent the first work on spin wave instability over the full FMR profile and the measurement of full butterfly curves for resonance saturation in metal films.

Section II gives an overview of the thin film materials, the low power microwave characterizations, the FMR system, and the measurement procedures. Section III introduces the high and low power FMR responses and gives details on the decoupling of the cavity and general calibration issues. Section IV presents the experimental results on resonance saturation. This includes representative calibrated data on microwave loss as a function of the microwave field amplitude, Suhl threshold determinations, and butterfly curves. Section V (1) gives a brief review of the uniform mode and spin wave theory modified for thin films, (2) provides a conceptual introduction to second order Suhl instability theory for thin films, and (3) develops the working h_{crit} equations and operational procedures for the evaluation of butterfly curves. Section VI considers the theoretical butterfly curve fits to the data, along with a discussion of the spin wave linewidths, damping parameters, and maximum precession angles at FMR that come from the analysis. Section VII provides a summary and conclusion.

II. THIN FILM MATERIALS AND MEASUREMENT PROCEDURES

A. Thin film materials and characterization

Permalloy films with thicknesses (d) of 35–123 nm were thermally evaporated on glass substrates in a nominal vacuum of 10^{-6} Torr and in the presence of an in-plane static field. The films evidenced the usual field induced uniaxial anisotropy with effective anisotropy fields in the range of 5 Oe or so. This anisotropy plays no critical role in the response of interest at fields around 800 Oe. Two of the films, with d values of 35 and 104 nm, were deposited on substrates held at ambient room temperature. Three films, with thicknesses of 57, 74, and 123 nm, were deposited on heated substrates at about 300 °C. All films were 5 mm in diameter and had nominal compositions of 82 at. % Ni and 18 at. % Fe. The films were all prepared by S. Konishi, Kyushu University, Fukuoka, Japan in the 1970s. In spite of the age of these films, the FMR profiles were all clean and reasonably narrow.

The basic film properties were determined by standard low power FMR measurements for both in-plane static field (IPSF) and perpendicular-to-plane static field (PPSF) configurations. Measurement details are given in the next section. Table I lists key results. The in-plane and out-of-plane FMR field values (H_{FMR}) were used to determine the effective saturation induction $4\pi M_{s\text{-}eff}$ and the gyromagnetic constant $\lvert\gamma\rvert/2\pi$ from the standard Kittel formula with the small uniaxial anisotropy ignored. The table lists the measured FMR fields for convenient transfer to the computed $4\pi M_{s\text{-}eff}$ and $\lvert\gamma\rvert/2\pi$ parameters shown. The listed $4\pi M_{s\text{-}eff}$ and $\lvert\gamma\rvert/2\pi$ values match reasonably well to literature values for the saturation induction and the gyromagnetic constant for Permalloy.

The last two columns show the measured half power FMR linewidths (ΔH_{FMR}) and the corresponding Gilbert damping parameters (α_{FMR}) for the measured films. These damping values were obtained from the standard connection derived from the Gilbert damped equation of motion, $\alpha_{FMR} = \lvert\gamma\rvert\Delta H_{FMR}/2\omega_p$, where $\omega_p/2\pi$ corresponds to the cavity frequency of 9.11 GHz. The reasonably small linewidths and low α_{FMR} values are indicative of good quality low loss films. The base parameters in Table I will be important for the analyses in later sections. The quantities listed, as well as parameters and equations to follow, are in Gaussian cgs units. Measurement details follow in the next section. Experimental results will focus on the 104 nm film.

B. FMR system and measurement procedures

All measurements were made with an X-band pulsed microwave reflection cavity spectrometer system similar to that described in Ref. 9. The empty TE102 cavity had a nominal center frequency $f=\omega_p/2\pi$ of 9.11 GHz, a power reflection coefficient ρ_0 of −30 dB at cavity resonance, and a loaded quality factor Q_L of 2600. The cavity was undercoupled and had a nominal empty cavity calibration coefficient $C_e = h^2/P$ of 3.54 Oe^2/W, where h is the amplitude of the microwave field for sample placement at the cavity end wall and P is the peak input power to the cavity. The setups were such that the linearly polarized microwave field was always in the plane of the film.

Downloaded 26 Jul 2007 to 129.82.208.99. Redistribution subject to AIP license or copyright, see http://jap.aip.org/jap/copyright.jsp

The high power capability was provided by a low duty cycle 8–18 GHz traveling wave tube amplifier with a peak power capability of 2 kW. All high power data were obtained in the IPSF configuration, with 4 μs wide linearly polarized input pulses at a 40 Hz repetition rate, peak powers up to 1 kW, and with the film samples placed on the cavity end wall. The duty cycle was set low enough to avoid sample heating effects. All of these measurements were made with 12 in. diam magnet pole pieces, a 5 in. magnet gap, and a corresponding high homogeneity static field at the sample position. The field change from the sample position to the position of the Hall probe used for the field measurement, about 1 cm away, was less than 0.2 Oe.

Two types of microwave measurements were made: (I) uncalibrated FMR absorption profiles of cavity voltage reflection coefficient ρ versus static magnetic field H for a range of peak power P values and (II) uncalibrated (II-u) and calibrated (II-c) threshold curve profiles of ρ vs P for a range of H values over the full FMR profile. The term "uncalibrated" means that the data were obtained under cavity loading conditions for which the connection between P and h was not fixed. This is generally the case when the static and microwave fields are mutually perpendicular and the FMR coupling is strong. Through a reduction in the coupling angle θ between these fields, the coupling can be reduced to the point where one can define $C=h^2/P$ for the sample loaded cavity and transition to a "calibrated" measurement. As a rule of thumb, one can calibrate the microwave field-power response as long as (1) the change in the cavity Q_L over the resonance line is less than 20% and (2) one performs the calibration as a function of ρ.

The type I ρ vs H measurements were used for the low power FMR position and linewidth determinations for both the IPSF and the PPSF configurations. The microwave field coupling angle θ was held at 90° in all cases. Even though the use of this maximum coupling means that the ρ vs H profiles are uncalibrated, the half power linewidths extracted from the profiles are still accurate. This was confirmed from actual response simulations based on the loaded cavity response. The low power IPSF FMR position and linewidth measurements were made at $P=0.44$ W and the same pulse width and repetition rate as given above. The corresponding low power PPSF measurements were made with $P=0.44$ W and 10 μs wide input pulses. For the PPSF measurements, fields in excess of 10 kOe were needed. It was necessary to place the samples on the sidewall of the cavity and fit the electromagnet with tapered pole pieces. The field change in this case from the Hall probe to the sample position was on the order of 0.75 Oe. The fields shown in Table I for both IPSF and PPSF FMRs, as well as the values given in the results below, show the corrected field values at the sample position, with an estimated accuracy of an oersted.

Types I and II measurements were both used for the IPSF configuration high power work. First, uncalibrated type I ρ vs H profiles as a function of power were used to survey the changes in the FMR absorption curve response with P. These results will be considered in Sec. III A. Second, type II-u (uncalibrated) ρ vs P threshold curve data for H values close to resonance and different coupling angles were used to determine the maximum coupling for a calibrated response. These coupling considerations and related calibration issues are given in Sec. III B. Finally, type II-c (calibrated) ρ vs P data were obtained for a full range of fields over the FMR profile for a small enough coupling angle, typically at $\theta \approx 60°$, to ensure a calibrated connection between P and h. These data, in turn, were used to obtain the threshold h_{crit} values as a function of H, the so-called butterfly curves introduced in Sec. I. As already noted, all of these data were obtained with the film sample on the end wall of the cavity with the microwave and static fields both in plane.

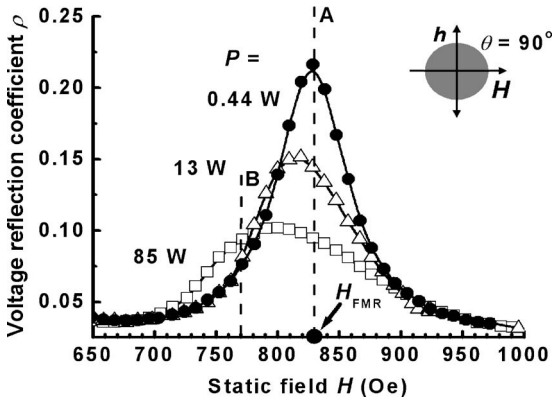

FIG. 1. Voltage reflection coefficient ρ vs the static external magnetic field H for the 104 nm thin film, the in-plane static field configuration, and a microwave frequency of 9.11 GHz. The symbols show data for different peak input power P values, as indicated. The dashed lines show cuts at 830 Oe, the ferromagnetic resonance field H_{FMR} line cut A, and B at a lower field value of 770 Oe. The H field and the linearly polarized microwave field h were in plane and mutually perpendicular at $\theta=90°$, as shown in the inset.

Sections III and IV are intended to provide a step-by-step development of the overall high power analysis procedure. This starts (Sec. III A) with the general effect of high power on the ρ vs H FMR profiles. This is followed (Sec. III B) with an analysis of ρ vs P data for a fixed field cut at the FMR peak to establish maximum coupling limits for a calibrated response. Appendix A then gives technical details on the procedure to obtain the cavity calibration parameter $C=h^2/P$. This parameter has meaning only in the low coupling limit. Section IV then uses data on ρ vs h to determine threshold field values (Sec. IV A) and develop butterfly curves of h_{crit} vs H (Sec. IV B).

III. QUALITATIVE FMR RESPONSE PROFILES AND MICROWAVE FIELD CALIBRATION

A. FMR response as a function of power

Figure 1 shows example uncalibrated FMR response profiles for the 104 nm film. The graph shows data on the cavity reflection coefficient ρ versus static field H for peak input power levels to the cavity (P) of 0.44, 13, and 85 W, as indicated. The static and microwave fields were in plane and mutually perpendicular at $\theta=90°$, as shown in the diagram inset. The vertical dashed line at the FMR field, labeled A, and the off resonance line, labeled B, correspond to H values of 830 and 770 Oe, respectively. These lines show ρ vs P cuts at fixed H that will be useful for the discussion in Sec. IV. It is important to emphasize that these FMR curves are

Downloaded 26 Jul 2007 to 129.82.208.99. Redistribution subject to AIP license or copyright, see http://jap.aip.org/jap/copyright.jsp

obtained at full coupling ($\theta=90°$) and there is no one-to-one correspondence between P and the microwave field amplitude h over a given profile. In other words, constant P does not mean fixed h.

As noted, the low power FMR peak in Fig. 1 is at 830 Oe and the half power linewidth is about 59 Oe. The qualitative changes in the profiles as P is increased provide an indication of the overall nonlinear response. The profile for $P=13$ W is broader, lower in amplitude, and slightly asymmetric, relative to the low power profile. The asymmetry amounts to a shift of the profile to lower fields and a development of a low field shoulder. This trend continues to an even greater extent for the $P=85$ W profile.

The drop in amplitude and broadening of the FMR peak with increasing power is the basic resonance saturation (RS) response associated with second order Suhl SWI processes. It is important to keep in mind that such processes occur for power levels well below those for which saturation effects are expected from classical theory. It is also important to note that the change in ρ with increasing power at a fixed field is not a continuous effect. Calibrated data on ρ vs h, to be considered shortly, will show that the change in reflection coefficient occurs more or less abruptly at some threshold h value. It is this change that defines the threshold microwave field amplitude h_{crit}.

The shift to low field and the development of the low field shoulder with increasing power is the manifestation of a foldover effect for metal films. The asymmetry development also leads to a kink in the butterfly curve, h_{crit} vs H profile, at a field somewhat below the minimum H point. The foldover shifts the high field response to a lower field and the nonlinear broadening increases the high field response to higher fields. The combination of these produces high field responses that appear to be independent of power with no measurable threshold. Preliminary work suggests that the foldover is due to two magnon scattering interactions.[11] Further work on two magnon effects in RS processes will be published separately.

B. Cavity calibration

As noted, accurate cavity calibration is critical to precise h_{crit} determinations. Before calibrations can be made, however, it is necessary to determine the maximum allowable FMR coupling for perturbation theory to be applicable. Once this limit is set, the coupling can be reduced to acceptable levels and the actual calibration coefficient C as a function of ρ can be obtained.

The upper limit on the FMR coupling for a valid calibrated response was determined from data on ρ vs P for different coupling angles (θ) between the microwave field and the static magnetic field. These data were obtained for a static field at the low power FMR peak. For comparison purposes the ρ data were converted to a reduced loss parameter L_R according to

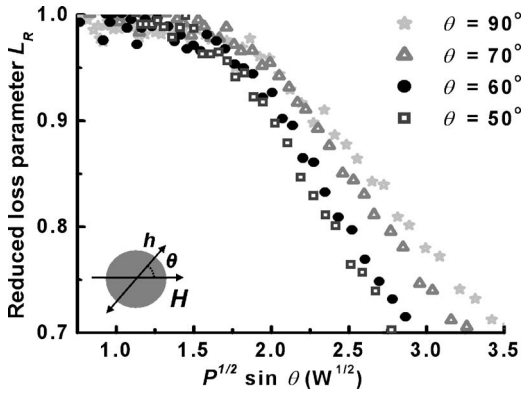

FIG. 2. Reduced loss parameter L_R vs the effective pumping factor $\sqrt{P}\sin\theta$ for the 104 nm thin film, where P is the peak input power to the cavity and θ is the coupling angle between the static field H and the microwave field h, as shown in the inset. Both fields are in plane. The data are for $H=830$ Oe and a pumping frequency of 9.11 GHz.

$$L_R = \frac{(\rho_P - \rho_{ref})}{(\rho_0 - \rho_{ref})}\frac{(1-\rho_0)}{(1-\rho_P)}. \quad (1)$$

Here, ρ_P is the measured ρ value for the input peak power P value of interest and ρ_0 is the ρ value in the low power limit, with both obtained at the FMR field, while ρ_{ref} is the reference ρ value with the static field set far from the FMR field.

The introduction of a reduced loss parameter L_R for the data comparison for different coupling angles deserves brief comment. Recall that at or close to FMR, the voltage reflection coefficient ρ is comprised of two parts, the empty cavity part ρ_0 and the component related to the FMR loss. As demonstrated in Fig. 1, the component related to FMR decreases as the power is increased. A decrease in coupling has a similar effect. As a result, one cannot use ρ as a basis of comparison for different coupling angles.

The standard microwave perturbation theory analysis for a weakly coupled cavity indicates that L_R should correspond to the ratio of the high and low power negative imaginary components of the microwave susceptibility. In other words, in the small coupling limit for which perturbation theory is valid, plots of L_R versus the effective pumping field should all show the same nonlinear response. Recall that the microwave field amplitude h at the sample position scales with the square root of P and that only the component of **h** that is *transverse* to the static field drives the FMR response. For a given angle θ between **H** and **h**, the *effective* pumping field amplitude will scale with $\sqrt{P}\sin\theta$. A determination of the maximum allowable coupling angle in this step of the calibration procedure may be obtained from plots of L_R vs $\sqrt{P}\sin\theta$.

Figure 2 shows representative data on L_R vs $\sqrt{P}\sin\theta$ for the 104 nm film and a range of coupling angles that demonstrate the loading effects described above. These specific data are for $H=830$ Oe, at the FMR line cut A in Fig. 1. Data are shown for θ values of 90°, 70°, 60°, and 50°, as indicated, and input powers from 0 to 49 W. For the two largest θ values, 70° and 90°, excessive cavity loading gives a L_R vs $\sqrt{P}\sin\theta$ response that depends on the coupling and shows a larger distortion for higher powers. For the two smaller θ values, 50° and 60°, the L_R vs $\sqrt{P}\sin\theta$ response profiles are

Downloaded 26 Jul 2007 to 129.82.208.99. Redistribution subject to AIP license or copyright, see http://jap.aip.org/jap/copyright.jsp

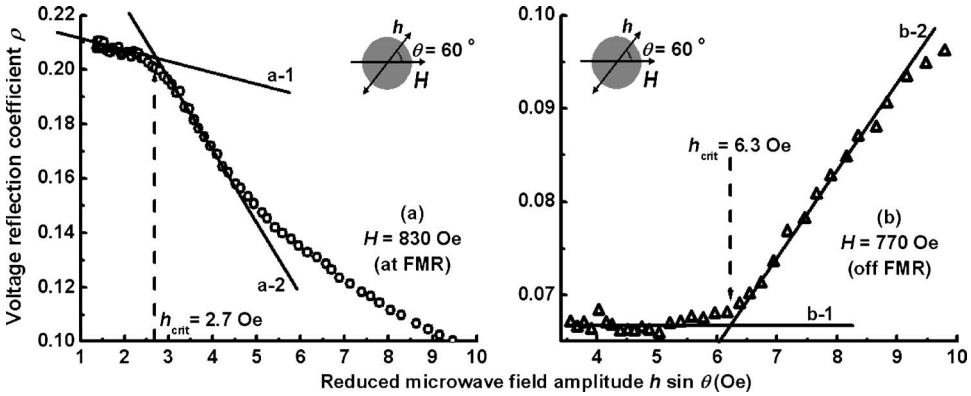

FIG. 3. Voltage reflection coefficient ρ vs the reduced microwave field amplitude $h \sin \theta$ for the 104 nm thin film at 9.11 GHz. The insets show the coupling geometry, with the in-plane static field H and the in-plane linearly polarized microwave field h at $\theta=60°$ for both sets of data. Graph (a) shows a representative threshold response for $H=830$ Oe, at the low power ferromagnetic resonance (FMR) peak position. Graph (b) shows the corresponding response for $H=770$ Oe, on the low field side of the low power FMR profile. The straight lines are guides to the eyes. The intersections marked by the vertical dashed lines give estimations of the spin wave instability threshold microwave field amplitude h_{crit} for the two different cases illustrated here.

identical within the error of the data. This is an indication that coupling angles at or below 60° or so are sufficient to put the cavity response in the regime where (1) perturbation theory is applicable and (2) a proper calibration between P and h is possible. Calibrated data on L_R vs $h \sin \theta$ in this regime give Suhl saturation response profiles that are independent of the coupling angle and give an accurate and reliable determination of the h_{crit} threshold at a given static field. It is also important to note that the change in the cavity Q_L over the full range of the data in Fig. 2 for the two *smallest* θ values is less than 20%. This is the order of change in coupling that sets an upper limit on the applicability of perturbation theory and a valid microwave field calibration.

Turn now to the determination of the calibration coefficient $C=h^2/P$ that connects the measured power P to the microwave field amplitude h. The traditional approach is to bias the cavity at a field far from ferromagnetic resonance and use the standard recipe from Ref. 11 for a determination of the various cavity parameters. This approach is inadequate for resonance saturation measurements. The changes in the cavity frequency, the Q_L parameters, and the calibration change substantially as one sweeps the static field across the full FMR profile. These changes make it impossible to obtain accurate h_{crit} values based on a single high field cavity reference measurement.

In the process to establish a workable calibration procedure, it was discovered that even though C changes as one moves across the FMR profile, this sought after calibration parameter is a unique function of the cavity reflection coefficient ρ. This is found to apply to all of the data for different samples, different coupling angles, and different static fields. The details of the procedure to determine the universal $C(\rho)$ calibration function are given in Appendix A. This calibration recipe represents a major improvement over previous work. With the exception of Ref. 9, most past FMR saturation measurements have been made for maximum coupling, that is, with perpendicular static and microwave fields. From Fig. 2, one can see that a large coupling can lead to a distortion in the threshold curve. This can result in an overestimation of the onset h value by as much as 10%. The calibration performed for this work, given in Fig. 5 (Appendix A), shows that the nominal off resonance C value of 3.54 Oe^2/W is 50% higher than the value at FMR. If this value is used for the h vs P calibration, the apparent microwave field values are about 25% too high. The combination of these considerations gives field calibration errors at FMR for the old off resonance approach in excess of 35%.

IV. HIGH POWER FERROMAGNETIC RESONANCE RESPONSE

As already noted, the change in the FMR response as the input microwave power level is increased is a threshold effect and not a gradual change. The threshold microwave field amplitude, previously defined as h_{crit}, is the subject of this section. Section IV A is concerned with the calibrated ρ vs $h \sin \theta$ responses obtained from the ρ vs P measurements at fixed static field, the change in these responses as one moves across the FMR profile, and the extraction of h_{crit} values from these data. Section IV B focuses on the butterfly curve profiles of h_{crit} vs H.

A. High power threshold response

Recall the two vertical A and B line cuts through the uncalibrated FMR profiles in Fig. 1. The A cut, at the low power FMR peak position, shows that the reflection coefficient decreases as the power is increased. The B cut, positioned well off the FMR peak, shows that ρ increases with an increase of power. Properly calibrated data based on the procedures given in Sec. III yield quantitative ρ vs $h \sin \theta$ plots that show the threshold effect.

Graphs (a) and (b) in Fig. 3 show calibrated ρ vs $h \sin \theta$ responses that correspond to the A and B field cuts at 830 and 770 Oe from Fig. 1. The insets show the H-h-θ coupling configurations. Recall that only the transverse component of **h** relative to the static field direction is effective in driving the response. The data are for the same 104 nm film and $\theta=60°$, as before. The straight lines provide guides to the eyes for the estimation of h_{crit} values from the data.

Downloaded 26 Jul 2007 to 129.82.208.99. Redistribution subject to AIP license or copyright, see http://jap.aip.org/jap/copyright.jsp

Both graphs demonstrate the threshold nature of the nonlinear response. For the FMR situation in (a), line a-1 shows that ρ is large and a weakly decreasing function of $h \sin\theta$ for low power and small h, while line a-2 shows a more rapid *decrease* at high power and large h. The intersection of the two lines defines the threshold h_{crit}. Off FMR, as in (b), the situation is different. Now, ρ is relatively small and essentially constant below threshold and then shows a rapid *increase* above threshold. In parallel with graph (a), lines b-1 and b-2 show the low and high power trends and the intersection that marks the h_{crit}. Note also that the threshold response is not particularly sharp in either case.

Figure 3 shows three things. First, both data sets show a threshold effect. The corresponding h_{crit} values can be taken to define a SWI threshold. The physical basis for the instability was established by Suhl in 1957.[2] The idea is that the driven uniform mode couples energy into parametrically pumped half frequency spin waves at a power dependent rate G_k. At the point in power at which G_k exceeds the relaxation rate of the spin waves, taken as η_k, the occupation numbers of the spin waves increase above thermal levels and one sees an abrupt change in the loss. A more detailed statement of the Suhl theory will be given in Sec. V.

Second, one sees quantitatively different threshold responses on and off resonance. At the low power FMR field position, as in (a), the change in the rate of decrease in ρ with increasing at $h \approx h_{crit}$ is due to an initial lockup in the FMR amplitude and a decrease in the effective microwave susceptibility. Off resonance, as in (b), the loss starts out small because the static field position is on the tail of the FMR response. As h exceeds h_{crit}, the parametric generation of spin waves leads to additional loss and ρ increases.

The third point to note is that the threshold transitions are fairly gradual and do not show the sharp threshold effects of the sort expected from the original nonlinear Suhl theory or in defect-free single crystal ferrites, for example. Suhl has also shown, however,[12] that two magnon scattering interactions can lead to this type of rounded response. As noted above, Krivosik[10] has extended the two magnon analysis of Suhl in the context of metallic thin films. Reference 10 shows that such processes can give a rounded rather than a sharp transition at threshold as well as the asymmetry in the high power FMR profile of the sort shown in Fig. 1.

B. Resonance saturation butterfly curves

Figure 4 shows a representative resonance saturation butterfly curve for the 104 nm thin film. The threshold fields were obtained from data similar to those in Fig. 3. At the high H limit of the data shown, the threshold responses were extremely weak or nonexistent. This is connected with the power independent high field FMR tail responses in Fig. 1. No reliable h_{crit} determinations were possible for static fields above about 880 Oe or so. The vertical line at H_X=810 Oe marks the threshold crossover point in field between the two types of responses shown in Fig. 3. The solid circle indicates the FMR field point from Table I. The solid curve shows a fit to the data based on the modified Suhl theory to be considered in Secs. V and VI.

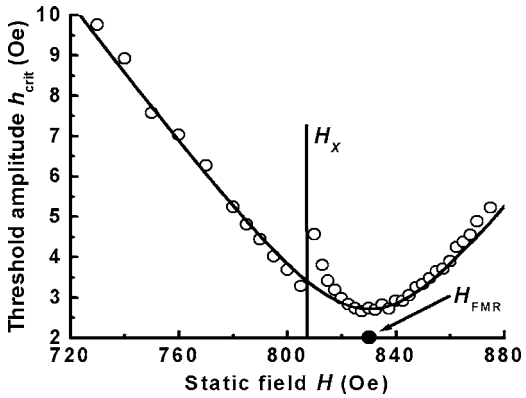

FIG. 4. Resonance saturation butterfly curve of the spin wave instability threshold microwave field amplitude h_{crit} vs static magnetic field H for the 104 nm thin film. The pumping frequency was 9.11 GHz. The coupling geometry is the same as in Fig. 3. The solid circle denotes the FMR field position. The vertical line at H_X marks the jump in the h_{crit} data. The solid curve shows a fit of the thin film second order spin wave instability theory to the data.

The data in Fig. 4 show two main features. First, the overall h_{crit} vs H profile shows a minimum threshold at the FMR field and a symmetric increase in the threshold as one moves to lower or higher fields. Second, there is a departure from the overall smooth symmetric profile for fields close to the H_X crossover point and a distinct jump in the h_{crit} vs H response at H_X.

The overall shape of the butterfly curve profile is tied closely to the low power FMR response. At the FMR peak where the FMR precession angle is large, the coupling to parametric spin waves is strong, and h_{crit} is at a minimum. As the static field is shifted above or below FMR, the precession angle decreases, the coupling also decreases, and a higher microwave field is needed to reach the instability threshold. Qualitatively, this means that the h_{crit} vs H profile is an inverted rendition of the low power FMR absorption profile. This connection is only qualitative because the actual coupling depends on the uniform mode response in a complicated way. The analytical formulas for the response are summarized below and in the Appendix. The good theoretical fit to the data shows that the rigorous analysis gives quantitative agreement.

As noted above, $H=H_X$ marks the crossover point in field between the two types of responses shown in Fig. 3. The deviation in the h_{crit} data from the smooth solid curve and the jump are related to the foldover effect in Fig. 1. Consider the situation for fields below H_X. In this regime, the shift of the broadened FMR profile to lower fields as the power is increased will correspond to a decrease in h_{crit}. For $H<H_X$, a higher ρ at a given field point in Fig. 1, compared to what one would have without a shift, corresponds to a lower threshold. The data in Fig. 4 do show a small drop in the threshold relative to the solid curve. Conversely, the higher ρ for $H_X<H<H_{FMR}$ causes an increase in threshold. For this field range, the data in Fig. 4 show a relatively large effect. The drop in h_{crit} for $H<H_X$ and the increase for $H>H_X$ then give the jump shown in the data.

The results given above for the 104 nm thin film are typical of the results for the other samples. Good theoretical

Downloaded 26 Jul 2007 to 129.82.208.99. Redistribution subject to AIP license or copyright, see http://jap.aip.org/jap/copyright.jsp

fits were obtained and all samples showed the same distortions and jump around the H_X point as just discussed.

V. SECOND ORDER SUHL SPIN WAVE INSTABILITY THEORY SUMMARIZED

Reference 8 outlines a simplified version of the Suhl spin wave instability theory for RS and subsidiary absorption (SA) processes in thin films but gives the working equations for the first order SA processes only. This section reviews the foundations of the theory, gives working equations that lead to the instability threshold microwave field amplitude h_{crit} and the corresponding critical modes for second order RS processes, and outlines an operational procedure for the analysis of RS butterfly curve data.

A. Uniform mode and spin wave basics

The starting point for the analysis is the magnetic torque equation of motion for the dynamic magnetization $\mathbf{m}(\mathbf{r},t)$,

$$\frac{d\mathbf{m}(\mathbf{r},t)}{dt} = -|\gamma|\mathbf{M}(\mathbf{r},t) \times \mathbf{H}_{\text{eff}}(\mathbf{r},t). \tag{2}$$

Here, $\mathbf{M}(\mathbf{r},t)$ represents the total magnetization and $\mathbf{H}_{\text{eff}}(\mathbf{r},t)$ is the total effective field. The magnetization is further expanded as

$$\mathbf{M}(\mathbf{r},t) = M_s\hat{\mathbf{z}} + \mathbf{m}_0(t) + \sum_{k\neq 0} \mathbf{m}_k(t)e^{-i(\mathbf{k}\cdot\mathbf{r}-\omega_k t)}, \tag{3}$$

where the M_s is the saturation magnetization, $\mathbf{m}_0(t)$ is the uniform mode part of the steady state dynamic magnetization response, and the $\mathbf{m}_k(t)e^{-i(\mathbf{k}\cdot\mathbf{r}-\omega_k t)}$ terms denote quasi-plane-wave spin wave excitations with an in-plane wave vector $\mathbf{k}$ and frequency ω_k. The total field, $\mathbf{H}_{\text{eff}}(\mathbf{r},t)$, is comprised of the external static magnetic field $\mathbf{H}=H\hat{\mathbf{z}}$, a uniform, transverse, in-plane, and linearly polarized microwave pumping field $\mathbf{h}_0(t)=h\cos(\omega_p t)\hat{\mathbf{x}}$, and the applicable uniform demagnetizing field, spatially varying dipole field, and effective exchange field.

For the thin film problem at hand, the $\hat{\mathbf{z}}$-directed static field is taken to be sufficient to saturate the film. The microwave field drives the uniform mode $\mathbf{m}_0(t)$ response. All of the $\mathbf{m}_k(t)$ spin wave amplitude factors are taken to be at thermal levels as long as one is below the Suhl instability threshold. The theory gives expressions for the threshold microwave field amplitude h_c at which some *particular* $\mathbf{m}_k(t)$ shows exponential growth. The $\mathbf{k}$ mode with the lowest threshold h_{crit} value is taken as the critical mode corresponding to some $\mathbf{k}_{\text{crit}}$. In principle, the corresponding threshold microwave field amplitude h_{crit} then corresponds to the SWI threshold.

The uniform mode response plays a key role. The standard linearized torque equation analysis in the small signal and low damping limit, with a uniform drive and damping included, yields specific expressions for $\mathbf{m}_0(t)$. The peak response is at the well known Kittel FMR frequency, $\omega_0(H)=|\gamma|\sqrt{H(H+4\pi M_s)}$. The condition $\omega_0(H)=\omega_p$ then defines the FMR field H_{FMR}. This is the field point indicated in Figs. 1 and 4. The critical low power experimental parameters are this FMR field and the half power linewidth ΔH_{FMR}, as introduced in Sec. II.

It is the $\mathbf{m}_0(t)$ response that drives the second order spin wave instability in the Suhl theory. The formulation is usually done in terms of a reduced transverse $\hat{\mathbf{x}}$-$\hat{\mathbf{y}}$ linear response function, written here as $a_0(t)=[m_{0x}(t)+im_{0y}(t)]/M_s$. From Eq. (2) with damping included, the working equation for $a_0(t)$ may be written as

$$a_0(t) = \frac{|\gamma|h}{2}(q_L e^{+i\omega_p t} + q_A e^{-i\omega_p t}), \tag{4}$$

where the q_L and q_A amplitudes denote the Larmor and the anti-Larmor contributions to the response and are

$$q_L = \frac{\omega_H + \omega_M + \omega_p}{\omega_0^2 - \omega_p^2 + i2\omega_p\eta_0} \tag{5}$$

and

$$q_A = \frac{\omega_H + \omega_M - \omega_p}{\omega_0^2 - \omega_p^2 - i2\omega_p\eta_0}. \tag{6}$$

The frequency parameters ω_H and ω_M, defined as $|\gamma|H$ and $|\gamma|4\pi M_s$, respectively, express H and $4\pi M_s$ in frequency units. The relaxation rate parameter η_0 is given by

$$\eta_0 = \frac{|\gamma|\Delta H_{\text{FMR}}}{2}\varepsilon, \tag{7}$$

where $|\gamma|\Delta H_{\text{FMR}}/2$ expresses the half power FMR linewidth as a decay or relaxation rate in frequency units. The multiplier ε is equal to $|\gamma|(2H_{\text{FMR}}+4\pi M_s)/2\omega_p$ and represents an ellipticity correction.[13] For Permalloy films at 10 GHz, this factor is about 2. The above formulas apply to isotropic in-plane magnetized films.

Turn now to the spin wave components denoted by the $\mathbf{m}_k(t)$ terms in Eq. (3). If one includes only linear spin wave terms in the torque equation analysis with no damping and works in the small signal limit with $|\mathbf{m}_k| \ll M_s$, one can obtain the spin wave dispersion relation written here as

$$\omega_k(\mathbf{k}) = |\gamma|\{[H + Dk^2 + 4\pi M_s(1-N_k)\sin^2\theta_k](H + Dk^2 + 4\pi M_s N_k)\}^{1/2}. \tag{8}$$

The D parameter denotes an effective exchange stiffness field,[13] $4\pi M_s N_k$ represents an effective dynamic dipole-dipole field, and θ_k is the angle between the in-plane $\mathbf{k}$ vector and the $\hat{\mathbf{z}}$-directed static field. For Permalloy, D may be taken as 2.1×10^{-9} Oe cm^2/rad^2.[14] Keep in mind that the wave vector $\mathbf{k}$ is constrained to the $\hat{\mathbf{x}}$-$\hat{\mathbf{z}}$ film plane. Following Harte,[15] the N_k function may be written as

$$N_k = (1 - e^{-kd})/kd. \tag{9}$$

Recall that d denotes the film thickness. The above relations apply (1) in the magnetostatic limit with wave numbers much larger than the corresponding pure electromagnetic wave k value at $\omega_k=\omega_p$ and (2) under the assumption that $kd \ll 1$ is valid and $\mathbf{m}_k(t)$ is uniform across the film thickness.

Reference 8 gives a detailed discussion of the spin wave dispersion relation in Eq. (8) and the role of the correspond-

Downloaded 26 Jul 2007 to 129.82.208.99. Redistribution subject to AIP license or copyright, see http://jap.aip.org/jap/copyright.jsp

ing spin wave band in SA processes. The main difference for RS processes is twofold. First, the relevant spin wave modes are at $\omega_k=\omega_p$ rather than at $\omega_k=\omega_p/2$. Second, the range of fields is limited to those close to the FMR field and the frequency shift of the spin wave band is *much smaller* than that for SA processes. For all practical purposes, one can shift all of the spin wave band diagrams in Fig. 4 of Ref. 8 so that the $k=0$ convergence point is at 9.11 GHz, and draw a horizontal line across the band through this point to define the range of allowed spin wave modes for resonance saturation.

B. Resonance saturation second order processes

The Suhl spin wave instability theory has been recast in various forms by Schloemann,[16] Schloemann *et al.*,[17] Patton,[18,19] Chen and Patton,[20] and Nazarov *et al.*,[21] among others. In brief, the magnetic torque equation of motion without damping can be taken and the (1) linear terms in $\mathbf{m}_k(t)$ and (2) higher order terms that include products of $\mathbf{m}_k(t)$ and uniform mode amplitudes as well as direct pumping field terms can be considered. As with the uniform mode, it is also convenient to convert the transverse $\hat{\mathbf{x}}$-$\hat{\mathbf{y}}$ part of $\mathbf{m}_k(t)$ into a reduced scalar complex amplitude $a_k(t)=[m_{k,x}(t)+im_{k,y}(t)]/M_s$. Spin wave damping is added at the end of the analysis through the replacement $\omega_k \rightarrow \omega_k+i\eta_k$. The η_k corresponds to the spin wave relaxation rate for the given mode at $\mathbf{k}$ and ω_k. In parallel with the $\eta_0=\varepsilon|\gamma|\Delta H_{\mathrm{FMR}}/2$ connection, it is useful to cast η_k in terms of a spin wave linewidth parameter $\Delta H_k=2\eta_k/|\gamma|$ that expresses the spin wave relaxation rate in linewidth units. Note that no ellipticity factor has been incorporated into this connection, so that ΔH_k is not a true linewidth but, rather, serves one simple function to cast η_k into linewidth units.

The final result for second order Suhl processes is a solution for the $a_k(t)$ that takes the form

$$a_k(t)=a_{k0}e^{\beta_k^{(2)}t}, \tag{10}$$

where $\beta_k^{(2)}$ is an exponential growth or decay parameter given by

$$\beta_k^{(2)}=\sqrt{|G_k^{(2)}|^2-(\omega_k-\omega_p)^2}-\eta_k. \tag{11}$$

In general, $G_k^{(2)}$ is one of several functions that prescribe the coupling between the uniform mode and a given spin wave mode at $\mathbf{k}$ and ω_k. The $G_k^{(2)}$ scales with the square of the uniform mode amplitude and, hence, with h^2. The fact that the coupling scales with the square of the uniform mode amplitude is the origin of the "second order" label for this particular Suhl process. Details of the analysis may be found in the above cited references.

The form of $\beta_k^{(2)}$ shows the instability effect even without a detailed knowledge of the $G_k^{(2)}$ function. For a sufficiently small h, $G_k^{(2)}$ will be small, $\beta_k^{(2)}$ will be negative, the $a_k(t)$ will always show a decay, there will be no spin wave instability, and the spin wave modes will continue to reside at thermal levels. As h is increased, however, $G_k^{(2)}$ will grow. At the point where $\beta_k^{(2)}$ becomes positive for some mode or set of available $(\mathbf{k},\omega_k)$ modes, there will be a threshold for the exponential growth in the $a_k(t)$ for these modes. In the experiment, one will see an effect for the particular set of $(\mathbf{k},\omega_k)$ modes with the *lowest threshold*. From Eq. (11), one can see, at the outset, that modes with $\omega_k=\omega_p$ will have a lower $G_k^{(2)}$ than other modes. Subject to this condition, the threshold condition for the unstable growth of parametric spin waves at $\omega_k=\omega_p$ reduces to the relatively simple form $G_k^{(2)}=\eta_k=|\gamma|\Delta H_k/2$.

Apart from the quadratic dependence on h, $G_k^{(2)}$ is in general not a simple function. In order to obtain an h_{crit} determination from the threshold condition, it is useful to separate out the h^2 part of the $G_k^{(2)}$ function according to

$$G_k^{(2)}(k,\theta_k)=\frac{(|\gamma|h)^2}{8\omega_p}W_k^{(2)}(H,k,\theta_k). \tag{12}$$

The new dimensionless $W_k^{(2)}(H,k,\theta_k)$ function includes the remaining dependences on the static field H, the spin wave propagation parameters k and θ_k, and all of the other parameters enumerated above. An explicit recipe for $W_k^{(2)}\times(H,k,\theta_k)$, as obtained directly from the Suhl theory adapted for thin films, is given in Appendix B. The algebra follows from the citations listed above and only the final results in compact form are given in Appendix B.

From the above form, one can see that the theoretical threshold $h_c^{(2)}$ for a general $\mathbf{k}$ mode will be given as $h_c^{(2)}=2[(\omega_p/|\gamma|)\Delta H_k/W_k^{(2)}(H,k,\theta_k)]^{1/2}$. At a given H, the available k and θ_k values will be defined by the $\omega_k(\mathbf{k})$ dispersion relation of Eq. (8), again subject to the $\omega_k=\omega_p$ constraint. The minimum threshold $h_{\mathrm{crit}}^{(2)}$ that corresponds to the measured h_{crit} is then obtained as the minimum value of $h_c^{(2)}$ among all of the available modes at $\omega_k=\omega_p$.

$$h_{\mathrm{crit}}^{(2)}=2\ \min\left[\sqrt{\frac{\omega_p\Delta H_k}{|\gamma||W_k^{(2)}(H,\theta_k)|}}\right]_{\omega_k=\omega_p}. \tag{13}$$

The separate k and θ_k parameters have now been replaced by a single θ_k variable. This is because the dispersion constraint, $\omega_k(k,\theta_k)=\omega_p$, allows one to write θ_k as a function of k.

For the present purposes, the spin wave linewidth parameter ΔH_k will be treated as a constant. In general, the spin wave relaxation rate η_k and the corresponding ΔH_k parameter can be a function of the spin wave frequency and wave vector $\mathbf{k}$. From the butterfly curve fits to be considered shortly, it will become clear that it is not necessary to consider such dependences explicitly in order to match the thin film Suhl theory to the present data. In contrast, this is usually not the case for first order processes.[8,13] Further comments on this point are given in the next section.

The numerical minimization procedure to obtain a theoretical $h_{\mathrm{crit}}^{(2)}$ for a given H is discussed at length in Ref. 21 and elsewhere. One starts with a fine mesh of the available θ_k values defined by the $\omega_k(k,\theta_k)=\omega_p$ constraint, evaluates the resulting $h_c^{(2)}$ at each point, and selects the minimum value of $h_{\mathrm{crit}}^{(2)}$. At the same time, the values of θ_k and k at this minimum threshold point define the critical mode propagation angle $\theta_{k\text{-crit}}$ and wave number k_{crit}. One then repeats the process for the field range of interest and constructs a theoretical butterfly curve of $h_{\mathrm{crit}}^{(2)}$ vs H as well as predicted field profiles

Downloaded 26 Jul 2007 to 129.82.208.99. Redistribution subject to AIP license or copyright, see http://jap.aip.org/jap/copyright.jsp

TABLE II. Summary of parameters for the fits of the Suhl theory to the resonance saturation butterfly curve data for all samples.

Film thickness n (nm)	Static field at the butterfly curve minimum H_{BC}^{min} (Oe)	In-plane static field (IPSF) FMR half power linewidth ΔH_{FMR} (Oe) (from Table I)	Spin wave linewidth (relaxation rate η_k in linewidth units) $\Delta H_k = 2\eta_k/\lvert\gamma\rvert$ (Oe)	Equivalent FMR Gilbert damping parameter α_{FMR}	Spin wave Gilbert damping parameter α_k	In-plane precession angle θ_{FMR}^{crit} (deg)
35	808	44	35	0.0072	0.0046	5.5
57	841	41	17	0.0066	0.0026	3.7
74	787	37	16	0.0060	0.0025	3.5
104	830	59	32	0.0093	0.0050	4.9
123	852	56	30	0.0090	0.0048	4.9

for $\theta_{k\text{-crit}}$ and k_{crit}. This entire process may be repeated with ΔH_k as a control parameter to obtain a best fit to a given experimental h_{crit} vs H profile. One can use such a fit to make an empirical determination of ΔH_k.

VI. BUTTERFLY CURVE FITS AND IMPLICATIONS

Figure 4, as discussed in Sec. IV B, gives representative butterfly curve data for the 104 nm film. The solid curve shows a fit to the data based on the theory summarized in Sec. V. The fit is based on the film parameters listed in Table I, the D value from Sec. V A, and a constant spin wave relaxation η_k value of 2.8×10^8 1/s. Recall that the conversion $\Delta H_k = 2\eta_k/\lvert\gamma\rvert$ is used to cast η_k in convenient linewidth units. The conversion gives $\Delta H_k = 32$ Oe. For reference, the corresponding Gilbert damping parameter, $\alpha_k = (\eta_k/\omega_k)/(\partial\omega_k/\partial\lvert\gamma\rvert H)$, is about 0.005.

The computed $h_{crit}(H)$ response shown in Fig. 4 is accompanied by critical mode k_{crit} and $\theta_{k\text{-crit}}$ vs H profiles. For the full range of static fields shown the critical mode propagation angles were at $\theta_{k\text{-crit}}=0°$. Interestingly, $\theta_{k\text{-crit}}=0°$ also comes out of the original Suhl SWI theory for bulk isotropic ferrites biased at the FMR field.[2] The corresponding k_{crit} values are in the small range 9.1×10^5–9.6×10^5 rad/cm, with the highest value at the low field limit of the data and the lowest value at the high field limit. Recall that the critical mode ω_k is equal to ω_p for second order processes, so that the $\theta_{k\text{-crit}}=0°$ determination in combination with Eq. (8) completely specifies $k_{crit}(H)$.

From Fig. 4, one can see that the thin film second order Suhl spin wave instability theory, with the spin wave relaxation rate or linewidth taken to be constant, gives a good match to the data. These RS butterfly curve data and the corresponding fits are only the second such results of record. The first such results, by Cox *et al.*,[9] were for in-plane magnetized single crystal Zn–Y-type hexagonal ferrite disks with planar anisotropy. For these samples, the Suhl theory with a constant η_k gave only a poor qualitative fit to the data. Good semiquantitative fits required the introduction of a substantial k-dependent component to the spin wave relaxation rate.

The ability to achieve a good theoretical fit to the experimental butterfly curve for a *single* η_k *value* in the case of metallic ferromagnetic films is likely due to the simple fact that the critical mode wave vector remains essentially constant over the full FMR profile. As noted above, the k_{crit} values are all limited to a very small range, 9.1×10^5–9.6×10^5 rad/cm, while the critical mode remains at $\theta_{k\text{-crit}}=0°$. The resultant shape of the theoretical butterfly curve is then determined only by the uniform mode susceptibility and the corresponding field dependent coupling factor $W_k^{(2)}(H,k,\theta_k)$ defined above and given in detail in the Appendix. In contrast, the changes in the critical mode k_{crit} and $\theta_{k\text{-crit}}$ values over the wide range of fields associated with the SA butterfly curve in An *et al.*[8] are substantial and the resultant fits to the SA butterfly curves were k dependent. Figure 6 in Ref. 8 shows, in particular, that the k_{crit} and $\theta_{k\text{-crit}}$ values range from about 1.5×10^5 to 3.0×10^5 rad/cm and from 0° to 17°, respectively.

Table II summarizes the results from similar fits for the full ensemble of films. Again, the fits are based on the film parameters listed in Table I and the D value from Sec. V A. The critical modes for all the fits were at $\theta_{k\text{-crit}}=0°$ and the corresponding narrow range of k_{crit} values defined by the $\omega_k=\omega_p$ constraint and the change in field. The fits for the 35 and 123 nm thick films were similar to that shown in Fig. 4 for $d=104$ nm. The data for the other two samples showed good fits for fields down to about 60 Oe or so below the butterfly curve minimum but poor fits for lower fields. For some reason, the measured h_{crit} values in this lower field range for these samples show a more rapid increase than the smooth data trend and corresponding theoretical response in Fig. 4.

The table gives results for all five samples. It lists the measured static fields at the butterfly curve minimum (H_{BC}^{min}), the FMR linewidths and α_{FMR} values from Table I, the spin wave linewidths (ΔH_k) and the Gilbert damping parameters (α_k) from the butterfly curve fits, and the in-plane FMR precession angles (θ_{FMR}^{crit}) at threshold. The Gilbert damping parameter associated with ferromagnetic resonance, α_{FMR}, is generally taken as the standard measure of the FMR loss. As such, the corresponding α_k parameter for spin waves can provide a useful basis for comparison here. The FMR precession angle at threshold is also a useful measure of the instability response. The initial effect as the microwave power exceeds the Suhl threshold is a lockup in the uniform mode precession cone at θ_{FMR}^{crit} as energy is pumped into spin waves. This angle, therefore, is an important parameter in spin wave instability processes.

Apart from the expected match up between the H_{BC}^{min} values and the IPSF H_{FMR} values in Table I, there are three main points to be made from the results in Table II. First, one can see that the spin wave Gilbert damping parameter α_k values

Downloaded 26 Jul 2007 to 129.82.208.99. Redistribution subject to AIP license or copyright, see http://jap.aip.org/jap/copyright.jsp

from the butterfly curve fits are lower, sometimes by a factor of 2 or more, than the corresponding FMR Gilbert damping parameter α_{FMR} values. Note that the α_{FMR} values in Tables I and II are based solely on the measured linewidths and the $\Delta H_{FMR}=2\alpha_{FMR}\omega_p/|\gamma|$ connection. These α_{FMR} values likely contain the effects of inhomogeneity and two magnon effects as well as the intrinsic magnon-electron scattering losses normally ascribed to the α parameter.[22,23] On the other hand, the generally lower α_k values are the result of the fact that the Suhl SWI derives from the renormalized mode with the lowest threshold. Renormalization can reduce, and in some cases eliminate, the broadening effects due to inhomogeneities, for example. The generally lower α_k values listed in the second to last column of Table II are in the 0.002–0.005 range nominally associated with intrinsic magnon-electron processes.[24–26]

Second, it is also important to note that two magnon scattering effects are expected to affect the extrapolated h_{crit} values of the sort shown in Fig. 3 to some degree. It was already noted in connection with Fig. 3 that the change from the expected abrupt transition at threshold to a rounded response is a two magnon effect. This introduces a certain level of ambiguity in any determination of a specific h_{crit} value. Any corresponding effect on h_{crit} will also modify the fitted α_k. For a complete threshold analysis that includes two magnon effects, it is necessary to include not only the nonlinear interactions between the uniform mode and spin wave modes but also the interactions between the parametric spin waves. These additional terms complicate the theory greatly. Zakharov and Lvov[27] and Cherepanov,[28] among others, have calculated the increase in threshold due to two magnon effects for first order Suhl SWI processes. But calculations have not been done for second order processes. Apart from a recent conference presentation,[10] however, there has been no detailed analysis of two magnon effects on second order RS instability processes. Such work is in progress.

The third and final point concerns the FMR precession angle just at the Suhl threshold, the lock-up angle θ_{FMR}^{crit}. The last column in Table II shows the calculated in-plane FMR precession angle just at threshold. One can see that this angle is generally in the range of a few degrees. As one moves above threshold, the lockup gradually relaxes, but there is a sizable increase in loss, well above the levels indicated by all of the ΔH_k and α_k parameters discussed above.[29] Large angle precession dynamics is an important element in many magnetic sensor and information storage applications, among others. Reference 1 describes one way to adapt Suhl theory to large angle switching dynamics. The present lock-up angle determinations provide a measure of the inherent limitations in a simple damped equation of motion analysis of large angle switching processes and the switching angle limits for the validity of such analyses.

VII. SUMMARY AND CONCLUSION

Resonance saturation FMR profiles have been measured as a function of microwave power and spin wave instability threshold h_{crit} measurements have been made over the full FMR absorption line for a series of Permalloy films at 9.11 GHz and room temperature. Careful attention to cavity loading and calibration issues has yielded the first comprehensive data on Suhl spin wave instability processes at FMR and over the full FMR profile for thin metal films. For each film, a theoretical analysis of the threshold data, based on the Suhl theory, suitably modified for thin films, yielded good fits to the butterfly curve data on h_{crit} versus in-plane static field H based on a single field independent value of the spin wave linewidth. These linewidths and the corresponding Gilbert damping parameter values are consistent with those expected for intrinsic magnon-electron relaxation. The implicit critical modes are consistent with the original Suhl theory and the FMR precession angles at threshold are quite small, on the order of few degrees.

These conclusions also raise several questions for future study. First, the evolution in the shapes of the FMR profiles with power and the apparent connections between these shapes and two magnon effects reported by Krivosik need further study. The second question, also related to two magnon effects, relates to the lack of a sharp threshold response and the rounded onset curves in Fig. 3. Finally, there are important questions about the response well above threshold and the connections between large angle switching processes, resonance saturation effects in FMR, and spin wave instability processes. The present results show that SWI processes result in a relatively small FMR precession lock-up angle. How are these processes connected to those that operate in large angle dynamics?

ACKNOWLEDGMENTS

This work was supported in part by the Information Storage Industry Consortium EHDR program, the Office of Naval Research, Grant No. N00014-06-1-0889, and the U.S. Army Research Office, Grant No. W911NF-04-1-0247. The late Professor S. Konishi of Kyushu University, Fukuoka, Japan provided the Permalloy films used in this work. Dr. Ralf Meckenstock, of the University of Duisberg-Essen, Germany, is acknowledged for helpful information on low linewidth films and intrinsic Gilbert damping values.

APPENDIX A

This appendix provides technical details on the determination of the calibration coefficient $C=h^2/P$. First, a point-by-point calibration of the cavity was done over the entire FMR profile, typically in 5–10 Oe steps, depending on the linewidth. Details on the determination of C in terms of the basic cavity parameters may be found in Refs. 11 and 30. These calibration data were then used to determine the C vs H response. As mentioned in Sec. III B, these C values, for a given cavity, are actually a *universal function* of the cavity reflection coefficient ρ. This means that one can use a universal $C(\rho)$ response function for all of the data for different samples, different coupling angles, and different static fields. This is also consistent with the $C=A(1-\rho)^2$ result from perturbation theory, where A is a known function of the cavity mode, cavity volume, and frequency.[11]

Figure 5 shows representative data for the 104 nm thin film at 9.11 GHz. The coupling angle was at $\theta=60°$, with

Downloaded 26 Jul 2007 to 129.82.208.99. Redistribution subject to AIP license or copyright, see http://jap.aip.org/jap/copyright.jsp

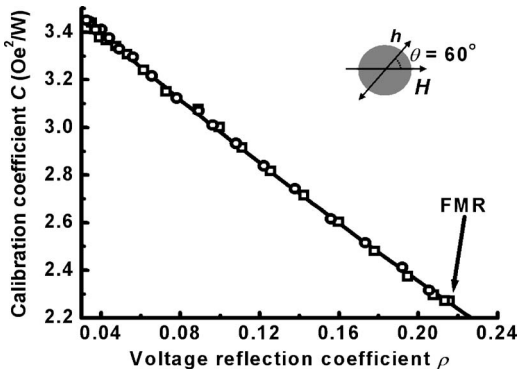

FIG. 5. Calibration coefficient C vs voltage reflection coefficient ρ for the 104 nm thin film at 9.11 GHz. The inset shows the coupling geometry, with the in-plane static field H and the in-plane linearly polarized microwave field h at a coupling angle θ of 60°, as indicated. The pumping frequency was 9.11 GHz. The data are for a cw microwave input power at about 10 dBm. The open square data points are for fields from 700 to 830 Oe and the open circle data points are for H values from 825 to 960 Oe. The arrow indicates the open square data point associated with the FMR peak. The solid line shows the theoretical response based on $C=A(1-\rho)^2$ with A set to 3.68 Oe^2/W.

both fields in plane as in the inset. The field ranged from 700 to 960 Oe. Recall that the low power FMR peak is at $H=830$ Oe. The cavity voltage reflection coefficient ρ ranged from about 0.22 at the FMR point to 0.03 at the high and low field end limits given above. The Q_L change over the range of the data was less than 20% and in line with the criteria established in Sec. III B. The data in Fig. 5 are shown in a C vs ρ format. For the undercoupled cavity, ρ is a maximum at the indicated FMR point. As one moves away from the FMR peak, either to lower or higher fields, ρ decreases. The open circles and squares correspond to fields above and below the FMR point, respectively. The solid line shows a best fit to the data, based on $C=A(1-\rho)^2$, with A taken as a single fitting parameter. The fit shown is for $A=3.68$ Oe^2/W. The χ^2 parameter for the fit was 0.000 13.

Figure 5 demonstrates two major points. First, the fact that the above resonance and the below resonance data fall on the *same* C vs ρ response curve provides proof that the universal $C(\rho)$ response function assumption is valid. Second, the fact that the data match the $C=A(1-\rho)^2$ relation provides further support for the thesis that perturbation theory is indeed applicable. The A value for the $C=A(1-\rho)^2$ fit is nominally the same as obtained from perturbation theory. For the nominal Q_L from the cavity calibrations and the cavity frequency, along with the volume and mode parameters for the cavity, one obtains a theoretical A value of 3.54 Oe^2/W.

Based on these results, one can see that a universal $C(\rho)$ function obtained either empirically or directly from perturbation theory is adequate for the cavity response calibration. The above procedure was repeated for all samples. In all cases, the same $C(\rho)$ calibration function was obtained.

APPENDIX B

This appendix gives working equations for the second order spin wave instability coupling coefficient $W_k^{(2)}$ needed for the h_{crit} analysis in Sec. V. This $W_k^{(2)}$ is written as

$$W_k^{(2)} = W_1 + W_2 + W_3 + W_4 + W_5. \tag{B1}$$

The W_1, W_2, W_3, W_4, and W_5 functions are given by

$$W_1 = q_L^2[r(A_k + \omega_p) - B_k v], \tag{B2}$$

$$W_2 = q_A^{*2}[r(A_k - \omega_p) - B_k v], \tag{B3}$$

$$W_3 = q_A^* q_L[s(A_k + \omega_p) + s(A_k - \omega_p) - B_k u], \tag{B4}$$

$$W_4 = \frac{1}{2} q_L (A_k + \omega_p - B_k), \tag{B5}$$

and

$$W_5 = \frac{1}{2} q_A^* (A_k - \omega_p - B_k). \tag{B6}$$

The A_k and B_k functions are given by

$$A_k = \omega_H + |\gamma| D k^2 + \frac{1}{2}\omega_M[(1 - N_k)\sin^2\theta_k + N_k] \tag{B7}$$

and

$$B_k = \frac{1}{2}\omega_M[(1 - N_k)\sin^2\theta_k - N_k]. \tag{B8}$$

The r, v, s, and u functions are given by

$$r = \frac{1}{4}\omega_M[(1 - N_k)2\cos^2\theta_k - 1] + \frac{1}{2}|\gamma| D k^2, \tag{B9}$$

$$v = \frac{1}{4}\omega_M, \tag{B10}$$

$$s = -\frac{1}{4}\omega_M[(1 - N_k)\sin^2\theta_k - (1 + N_k)], \tag{B11}$$

and

$$u = \frac{1}{2}\omega_M[(1 - N_k)(3\cos^2\theta_k - 1) - (1 + N_k)]. \tag{B12}$$

The q_L and q_A parameters correspond to the Larmor and anti-Larmor uniform mode response functions given in Sec. V. Also as defined in Sec. V, the ω_M and ω_H express $4\pi M_s$ and H in frequency units and are equal to $|\gamma|4\pi M_s$ and $|\gamma|H$, respectively.

[1] A. Yu. Dobin and R. H. Victora, J. Appl. Phys. **95**, 7139 (2004).
[2] H. Suhl, J. Phys. Chem. Solids **1**, 209 (1957).
[3] A. N. Slavin and P. Kabos, IEEE Trans. Magn. **41**, 1264 (2005).
[4] M. A. Hoefer, M. J. Ablowitz, B. Ilan, M. R. Pufall, and T. J. Silva, Phys. Rev. Lett. **95**, 267206 (2005).
[5] J. B. Comly, T. Penney, and R. V. Jones, J. Appl. Phys. **34**, 1145 (1963).
[6] A. Berteaud and H. Pascard, J. Appl. Phys. **36**, 970 (1965).
[7] A. Berteaud and H. Pascard, J. Appl. Phys. **37**, 2035 (1966).
[8] S. Y. An, P. Krivosik, M. A. Kramer, H. M. Olson, A. V. Nazarov, and C. E. Patton, J. Appl. Phys. **96**, 1572 (2004).
[9] R. G. Cox, C. E. Patton, M. A. Wittenauer, P. Kabos, and L. Chen, J. Appl. Phys. **89**, 4454 (2001).
[10] P. Krivosik, Technical Digests, IEEE International Magnetics Conference, San Diego, CA, 8–12 May 2006 (unpublished), Raytheon Tech. Report No, R-48.
[11] J. J. Green and T. Kohane, SCP Solid State Tech 7, 49 (1964).
[12] H. Suhl, J. Appl. Phys. **30**, 1961 (1959).

Downloaded 26 Jul 2007 to 129.82.208.99. Redistribution subject to AIP license or copyright, see http://jap.aip.org/jap/copyright.jsp

[13]C. E. Patton, in *Magnetic Oxides*, edited by D. J. Craik (Wiley, London, 1975), pp. 575–645.
[14]M. Nisenoff and R. W. Terhune, J. Appl. Phys. **36**, 732 (1965).
[15]K. J. Harte, J. Appl. Phys. **39**, 1503 (1968).
[16]E. Schloemann, Technical Abstract No. R-48, 1959 (unpublished).
[17]E. Schloemann, R. I. Joseph, and I. Bady, J. Appl. Phys. **34**, 672 (1963).
[18]C. E. Patton, Phys. Status Solidi B **92**, 211 (1979).
[19]C. E. Patton, J. Appl. Phys. **40**, 2837 (1969).
[20]M. Chen and C. E. Patton, in *Nonlinear Phenomena and Chaos in Magnetic Materials*, edited by P. E. Wigen (World Scientific, Singapore, 1994), Chap. 3.
[21]A. V. Nazarov, C. E. Patton, R. G. Cox, L. Chen, and P. Kabos, J. Magn. Magn. Mater. **248**, 164 (2002).
[22]S. S. Kalarickal, D. Menard, J. Das, C. E. Patton, X. Zhang, L. C. Sengupta, and S. Sengupta, J. Appl. Phys. **100**, 084905 (2006).
[23]V. Kambersky and C. E. Patton, Phys. Rev. B **11**, 2668 (1975).
[24]R. Meckenstock, D. Spoddig, Z. Frait, V. Kambersky, and J. Pelzl, J. Magn. Magn. Mater. **272**, 1203 (2004).
[25]Z. Frait and D. Fraitová, J. Magn. Magn. Mater. **15**, 1081 (1980).
[26]R. Meckenstock, O. von Geisau, J. Pelzl, and J. A. Wolf, J. Appl. Phys. **77**, 6439 (1995).
[27]V. Zakharov and V. S. Lvov, Sov. Phys. Solid State **14**, 2513 (1973).
[28]V. B. Cherepanov, Phys. Rev. B **45**, 12397 (1992).
[29]T. Gerrits, P. Krivosik, M. L. Schneider, C. E. Patton, and T. J. Silva, Phys. Rev. Lett. **98**, 207602 (2007).
[30]C. E. Patton and J. J. Green, Rev. Sci. Instrum. **42**, 193 (1971).

Downloaded 26 Jul 2007 to 129.82.208.99. Redistribution subject to AIP license or copyright, see http://jap.aip.org/jap/copyright.jsp